Miniature fiber-optic force sensor based on low-coherence Fabry-Pérot interferometry for vitreoretinal microsurgery

Xuan Liu,[1,*] Iulian I. Iordachita,[2] Xingchi He,[3] Russell H. Taylor,[2] and Jin U. Kang[1]

[1]*Department of Electrical and Computer Engineering, Johns Hopkins University, Baltimore, MD 21218, USA*
[2]*Laboratory for Computational Sensing and Robotics, Center for Computer-Integrated Surgical Systems and Technology, Johns Hopkins University, Baltimore, MD 21218, USA*
[3]*Department of Mechanical Engineering, Johns Hopkins University, 3400 N. Charles Street, Baltimore, MD 21218, USA*

*xliu35@jhu.edu

Abstract: During vitreoretinal surgery, the surgeon manipulates retinal tissue with tool-to-tissue interaction forces below the human sensory threshold. A force sensor (FS) integrated with conventional surgical tools may significantly improve the surgery outcome by providing tactile feedback to the surgeon. We designed and built a surgical tool integrated with a miniature FS with an outer diameter smaller than 1 mm for vitreoretinal surgery based on low-coherence Fabry–Pérot (FP) interferometry. The force sensing elements are located at the tool tip which is in direct contact with tissue during surgery and the FP cavity length is interrogated by a fiber-optic common-path phase-sensitive optical coherence tomography (OCT) system. We have calibrated the FS's response to axial and lateral forces and conducted experiments to verify that our FS can simultaneously measure both axial and lateral force components.

© 2012 Optical Society of America

OCIS codes: (050.2230) Fabry-Perot; (120.3180) Interferometry; (280.4788) Optical sensing and sensors; (120.5050) Phase measurement; (170.4500) Optical coherence tomography.

References and links

1. P. K. Gupta, P. S. Jensen, and E. de Juan, "Surgical forces and tactile perception during retinal microsurgery," in *Proceedings of the Medical Image Computing and Computer-Assisted Intervention—MICCAI'99*, Vol. 1679/1999 of Lecture Notes in Computer Science (Springer, 1999), pp. 1218–1225.
2. M. J. Massimino and T. B. Sheridan, "Sensory substitution for force feedback in teleoperation," IFAC Symp. Ser. **5**, 109–114 (1993).
3. M. Kitagawa, D. Dokko, A. M. Okamura, B. T. Bethea, and D. D. Yuh., "Effect of sensory substitution on suture manipulation forces for surgical teleoperation, " in *Medicine Meets Virtual Reality 12*, J. D. Westwood, R. S. Haluck, H. M. Hoffman, G. T. Mogel, R. Phillips, and R. A. Robb, eds. (IOS Press, 2004). pp. 157–163.
4. T. Akinbiyi, C. E. Reiley, S. Saha, D. Burschka, C. J. Hasser, D. D. Yuh, and A. M. Okamura, "Dynamic augmented reality for sensory substitution in robot-assisted surgical systems," in *28th Annual International Conference of the IEEE Engineering in Medicine and Biology Society, 2006. EMBS '06* (IEEE, 2006), pp. 567–570.
5. M. Balicki, A. Uneri, I. Iordachita, J. Handa, P. Gehlbach, and R. H. Taylor, "Micro-force sensing in robot assisted membrane peeling for vitreoretinal surgery," in *Medical Image Computing and Computer-Assisted Intervention—MICCAI 2010*, Vol. 6363/2010 of Lecture Notes in Computer Science (Springer, 2010), pp. 303–310.
6. A. Uneri and M. Balicki, J. Handa, P. Gehlbach, R. Taylor, and I. Iordachita, "New Steady-hand eye robot with microforce sensing for vitreoretinal surgery research," in *2010 3rd IEEE RAS and EMBS International Conference on Biomedical Robotics and Biomechatronics (BioRob)*, (IEEE, 2010), pp. 814–819.

7. Z. Sun, M. Balicki, J. Kang, J. Handa, R. Taylor, and I. Iordachita, "Development and preliminary data of novel integrated optical microforce sensing tools for retinal microsurgery," in *IEEE International Conference on Robotics and Automation, 2009. ICRA '09* (IEEE, 2009), pp. 1897–1902.
8. I. Iordachita, Z. Sun, M. Balicki, J. U. Kang, S. J. Phee, J. Handa, P. Gehlbach, and R. H. Taylor, "A sub-millimetric, 0.25 mN resolution fully integrated fiber-optic force-sensing tool for retinal microsurgery," Int. J. CARS **4**(4), 383–390 (2009).
9. K. Kim, Y. Sun, R. Voyles, and B. Nelson, "Calibration of multi-axis MEMS force sensors using the shape-from-motion method," IEEE Sens. J. **7**(3), 344–351 (2007).
10. A. Menciassi, A. Eisinberg, G. Scalari, C. Anticoli, M. C. Carrozza, and P. Dario, "Force feedback-based microinstrument for measuring tissue properties and pulse in microsurgery," in *IEEE International Conference on Robotics and Automation, 2001* (IEEE, 2001), pp. 626–631.
11. P. J. Berkelman, L. L. Whitcomb, R. H. Taylor, and P. Jensen, "A miniature microsurgical instrument tip force sensor for enhanced force feedback during robot-assisted manipulation," IEEE Trans. Robot. Autom. **19**(5), 917–922 (2003).
12. P. J. Berkelman, L. L. Whitcomb, R. H. Taylor, and P. Jensen, "A miniature instrument tip force sensor for robot/human cooperative microsurgical manipulation with enhanced force feedback," in *Medical Image Computing and Computer-Assisted Intervention—MICCAI 2000*, Vol. 1935/2000 of Lecture Notes in Computer Science (Springer, 2000), pp. 897–906.
13. D. Jagtap and C. N. Riviere, "Applied force during vitreoretinal microsurgery with handheld instruments," in *26th Annual International Conference of the IEEE Engineering in Medicine and Biology Society, 2004. IEMBS '04* (IEEE, 2004), pp. 2771–2773.
14. C. Yeh, *Handbook of Fiber Optics: Theory and Applications* (Academic, 1990), Chap. 11.
15. P. Puangmali, H. Liu, K. Althoefer, and L. D. Seneviratne, "Optical fiber sensor for soft tissue investigation during minimally invasive surgery," in *IEEE International Conference on Robotics and Automation, 2008. ICRA 2008* (IEEE, 2008), pp. 2934–2939.
16. S. Hirose and K. Yoneda, "Development of optical 6-axial force sensor and its signal calibration considering non-linear interference," in *1990 IEEE International Conference on Robotics and Automation, 1990. Proceedings* (IEEE, 1990), Vol. 1, pp. 46–53.
17. H. Su, M. Zervas, C. Furlong, and G. S. Fischer, "A miniature MRI-compatible fiber-optic force sensor utilizing Fabry-Perot interferometer," in *Conference Proceedings of the Society for Experimental Mechanics Series 2011, Volume 999999*, Vol. 4 of MEMS and Nanotechnology (Springer, 2011), pp. 131–136.
18. Y. Zhang, H. Shibru, K. L. Cooper, and A. Wang, "Miniature fiber-optic multicavity Fabry-Perot interferometric biosensor," Opt. Lett. **30**(9), 1021–1023 (2005).
19. U. Sharma, N. M. Fried, and J. U. Kang, "All-fiber Fizeau optical coherence tomography: sensitivity optimization and system analysis," IEEE J. Quantum Electron. **11**, 11799–11805 (2005).
20. J. U. Kang, J.-H. Han, X. Liu, K. Zhang, C. G. Song, and P. Gehlbach, "Endoscopic functional Fourier domain common path optical coherence tomography for microsurgery," IEEE J. Sel. Top. Quantum Electron. **16**(4), 781–792 (2010).
21. J. Zhang, B. Rao, L. Yu, and Z. Chen, "High-dynamic-range quantitative phase imaging with spectral domain phase microscopy," Opt. Lett. **34**(21), 3442–3444 (2009).
22. C. Joo, T. Akkin, B. Cense, B. H. Park, and J. F. de Boer, "Spectral-domain optical coherence phase microscopy for quantitative phase-contrast imaging," Opt. Lett. **30**(16), 2131–2133 (2005).
23. X. Liu, M. Balicki, R. H. Taylor, and J. U. Kang, "Towards automatic calibration of Fourier-Domain OCT for robot-assisted vitreoretinal surgery," Opt. Express **18**(23), 24331–24343 (2010).
24. M. Born and E. Wolf, *Principles of Optics* (Pergamon, 1964), Chap. 1.
25. A. Pytel and J. Kiusalaas, *Mechanics of Materials* (Brooks/Cole, 2003), Chap. 6.
26. R. D. Yates and D. J. Goodman, *Probability and Stochastic Processes* (Wiley, 2005), Chap. 5.

1. Introduction

Microsurgery involves the manipulation of very small anatomical structures. It is a series of manual manipulations performed predominantly using visual feedback, typically with the aid of a surgical microscope or other magnification device. In addition to visual feedback, tactile feedback can improve surgical outcome significantly. However, in microsurgical procedures such as vitreoretinal surgery, tool-to-tissue interaction forces are usually below human perception thresholds. Gupta et al. reported that 75% of tool-to-tissue interaction forces in vitreoretinal surgery were less than 7.5 mN in magnitude and that only 19% of force events at this magnitude were felt by the surgeon [1]. Although various tactile feedback or "sensory

substitution" schemes (e.g., [2–6]) may be used to provide feedback to the surgeon about these forces to help prevent potential tissue damage in freehand or robotic assisted surgery, a suitable force sensor (FS) must be incorporated into the surgical tools. In vitreoretinal surgery, the interaction forces between the tool and the sclera (white part) of the eye are often equal to or larger than the forces between the tool tip and the tissue being manipulated [7,8]. Thus, in addition to high sensitivity in force measurement, vitreoretinal microsurgery also requires using small size sensors that can be integrated into sub-millimetric instrument shafts. These considerations make the design of suitable force sensors for vitreoretinal microsurgery very challenging.

Previously, a MEMS technique and miniature strain gauge have been implemented in the development of micro force sensing tools for retinal microsurgery, such as 1 degree of freedom (DOF) pick-like FS developed by Gupta et al. [1], multi-axis MEMS FS developed by Kim et al. [9], microgripper-integrated FS developed by Menciassi et al. [10], 3 DOF FS developed by Berkelman et al. [11,12] which had been incorporated later into a hand-held instrument and used to measure forces in retinal tasks [13]. Most of the above-mentioned sensors, with the exception of that of Gupta et al. [1], are too large to be incorporated within a surgical tool that will be placed inside the eye during vitreoretinal microsurgery.

Force sensors based on fiber optics can be very small, mechanically stable, immune to electrical noise, and sterilizable [14]. Therefore they are ideal for incorporating into conventional surgical tools and for use as sensory substitution for tactile feedback in vitreoretinal microsurgery. Various force sensing schemes based on fiber optic techniques have been investigated over the last several decades. For example, FS that measures the change of optical power due to beam deflection has been developed for minimally invasive surgery [15,16]. However, such FS cannot be directly used in vitreoretinal microsurgery due to the large diameter (about several to ten millimeters) and low force sensitivity (several to tens of millinewtons). In our previous work [8], we incorporated fiber Bragg grating (FBG) sensors into the shafts of microsurgical instruments. Although this approach produces very high force sensitivity in directions that are perpendicular to the tool shaft (lateral directions), the axial rigidity of both the tool and fibers makes achieving high axial force sensitivity with FBG sensors a challenging problem. Fabry–Pérot interferometer (FPI) type sensors have also been used in bio-applications, including surgical force sensing [17,18]. The immediate advantage of FPI type micro force sensing is that it can potentially achieve a better axial sensitivity than that of FBG FS.

In this study, we designed and built a fiber optic FS consisting of Fabry–Pérot interferometer (FPI) cavities at the distal end of a fiber probe for potential applications in vitreoretinal surgery. In our FPI-FS, the length of FP cavity changed with force and we used a common-path Fourier domain optical coherence tomography (CP-FD-OCT) to interrogate the change of cavity length by phase-sensitive detection. The simple and compact common-path OCT configuration not only allows the use of optical probes with arbitrary lengths [19,20], but also provides improved phase stability to achieve sub-nanometer sensitivity in displacement measurement [21] and therefore to achieve high force sensitivity. Moreover, OCT also facilitates simultaneous measurement of multiple FP cavity lengths [22]. In our FS, we multiplexed three FPIs together to simultaneously obtain signals from three different channels. This enabled us to measure force in three dimensions with components both along and perpendicular to the tool shaft, which, to the best of our knowledge, has not been reported before.

In this manuscript, we present the designing and fabrication of our FPI-FS (Section 2). Principle of phase-sensitive detection and multidimensional force measurement are presented in Section 3. In Section 4, we summarize the results of tool calibration and show experimental results of measured force. The final sections are discussion and conclusion.

2. Principle and tool design

2.1. System overview and tool fabrication

Figure 1(a) shows the system schematic of FPI-FS for vitreoretinal microsurgery. The FP cavities that sense the forces are located at the tip of a conventional surgical tool—a surgical pick in this case—which is inserted into an eye to perform surgical tasks during vitreoretinal surgery. Detail of the FPI-FS probe is shown on the left side of Fig. 1(b). A CP-FD-OCT system is used to interrogate the length of the cavities by phase-sensitive detection. More details of our CP-FD-OCT system can be found in our previous work [23]. In brief, as shown on the right side of Fig. 1(b), it is a spectral-domain OCT system operating in 800 nm wavelength range with a ~6μm axial resolution and a ~3 mm imaging depth. The real-time 1-kHz data acquisition and processing was implemented with C++ in a Dell Precision T7400 computer.

In our FPI-FS system, a superluminescent emission diode (SLED, Exalos Inc.) is used as broadband source (BS) to illuminate three FPIs which consist of a shared end mirror and three lead-in single-mode fibers (SM800-5.6-125, Thorlabs, 125 μm cladding diameter). The mirror, which serves as the end reflector of the FPIs, was fabricated by polishing the surface of a stainless steel wire having 0.5mm diameter and 2.5mm length. We cleaved the fiber tips to right angle so the light is partially reflected at the fiber tip. Optical fields reflected by the fiber tips ($E_{1i}, i = 1,2,3$) and the metal reflector ($E_{2i}, i = 1,2,3$) are combined (as shown in Fig. 1(b)), routed through the coupler, and the interference signal is detected by the spectrometer.

As depicted in Fig. 1(b), the force-sensing part of the tool contained three optical fibers and a mirror, which form three FPIs with different cavity lengths. Other components of the FS include a tool shaft, a flexure, and a tool tip (pick). The tool shaft is made of a piece of titanium wire that is strong, lightweight, and biocompatible. The wire is 0.5 mm in diameter and 50 mm in length. Three square section channels (0.15 mm × 0.15 mm) were machined (laser cut) into the surface of the wire along the tool axis, $2\pi/3$ from one another in a circle, as shown in Fig. 1(c). Fibers were embedded and fixed into the channels.

The mirror and tool shaft are bound by a flexure made of Nitinol using a laser cut technique. The flexure deforms proportionally to the force applied and therefore induces change in the lengths of the FP cavities that will be used to calculate the force. We chose to use Nitinol because of its super-elastic property which enables the tool to have a measurable deformation with a force in the order of a millinewton. Nitinol has modulus of elasticity ranging from 41×10^3 MPa to 75×10^3 MPa; therefore, the fabricated tool has extremely high force sensitivity. As shown in Fig. 1(d), the flexure—with 0.80mm outer diameter (OD) and 0.60mm inner diameter (ID)—has five layers; each layer consists of three 40-micrometer struts; and between adjacent layers there is a 100 micrometer slot. The multi-layered configuration can further increase the elasticity of the flexure in the axial direction and therefore achieve a high sensitivity for force measurement. The total length of the flexure is 3 mm, with 1 mm between the distal end and the first slot. The pick was made using a stainless steel SS304 hypodermic tube, 21 gauge (OD = 0.80mm, ID = 0.55mm). The tip was bevel cut (at 75 degrees) and bent at around 45 degrees relative to the axis. The pick total length is 2.5mm, with a 1.5mm length bevel section. Loctite medical instant adhesive (Henkel, Dusseldorf, Germany) was used to bond all the parts together: first the mirror with the pick, next the flexure, and finally the tool shaft. The optical fibers were embedded into slots machined to the tool shaft. The distance between the fiber tips and the polished metal surface was manually adjusted before finally bonding the fibers with the tool shaft. It is worth mentioning that we made the FP cavities to have different lengths. This allows us to detect the length change of each cavity respectively. The CAD model for the FPI-FS probe integrated with the pick is shown in Fig. 1(e). For calibration and future manual or robotic use, the force sensing probe is attached to a custom-made handle, as shown in Fig. 1 (f). Figure 1(g) is a photo of the tool pictured below a U.S. quarter.
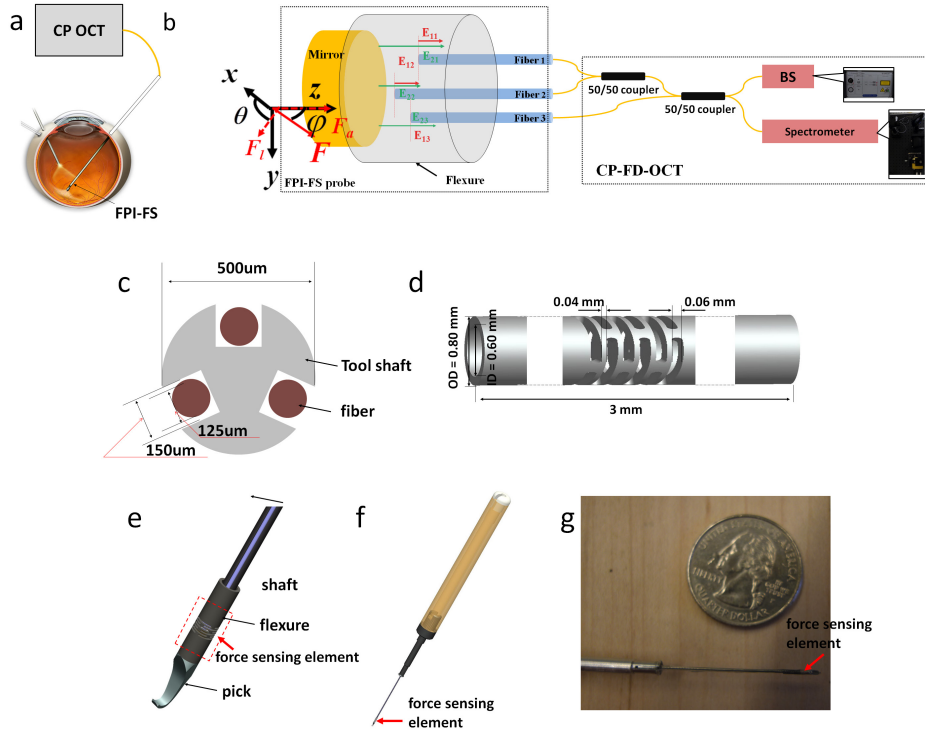
Fig. 1. (a) System schematic of FPI FS; (b) detailed schematic of the system including FPI-FS and CP OCT interrogation; (c) cross section of tool shaft with fiber embedded; (d) CAD model for the Nitinol flexure; (e) CAD model of the FPI-FS probe without the tool handle; (f) CAD model of the FPI-FS probe with the tool handle; (g) photo of the tool pictured below a US quarter.

2.2. OCT signal and phase-sensitive detection

Assuming that the polished metal surface reflects all the incident light and that the fiber tip reflectivity, *r,* is about 4% according to Fresnel equation [24], we calculated the finesse of the FPI to be about 1.25. The round trip loss of optical power in the FP cavity is larger than 4% due to beam divergence; therefore, the actual finesse of FPIs are even lower than 1.25. Moreover, we have measured the fringe visibility of interferograms obtained from the FPIs and the values are very small (0.39, 0.047 and 0.049, for three FPIs, respectively). Therefore, in our multiplexed FPIs, signals due to higher order reflections are small and therefore can be neglected in the following analysis.

As shown in Fig. 1(b), we denote the optical field reflected by the tip of the ith fiber as E_{1i}. We denote the optical field reflected by the shared end mirror and collected by the ith fiber as E_{2i} (i = 1,2, and 3). We have $E_{1i} = ra_iE_0(k)\exp(-jkl_i)$ and $E_{2i} = r_{2i}a_iE_0(k)\exp[-jk(l_i + 2L_i)]$. Here, j is the imaginary unit; $k = 2\pi/\lambda$ is the wavenumber; $E_0(k)$ is the spectral density of the broadband source; a_i is the portion of light that is coupled into the ith fiber from the source; r_{2i} takes into account both fiber coupling loss and the reflectivity of the polished metal surface; l_i is the round trip optical path length traveled within the ith fiber; L_i is the length of the ith FP cavity, which varies when there is force applied to the tool, as shown in Eq. (1):

$$L_i = L_{i,0} + \delta l_i (F).$$ (1)

In Eq. (1), $L_{i,0}$ is the length of ith FP cavity at neutral when there is no force exerted. δl_i indicates change of cavity length due to force exerted to the tool.

Since the round trip optical path length traveled within the ith fiber, l_i, varies significantly from other fibers (much more than several millimeters), E_{1i} or E_{2j} does not interfere if $i \neq j$. Based on this fact, the spectral interferogram $S(k)$ can be expressed as in Eq. (2):

$$S(k) = \eta \left[\sum_{i=1}^{3} \left| E_{1i}(k) \right|^2 + \sum_{i=1}^{3} \left| E_{2i}(k) \right|^2 + \sum_{i=1}^{3} 2\,\text{Re}\left(E_{1i}(k) E_{2i}^{\ *}(k) \right) \right] \qquad (2)$$

In Eq. (2), η indicates the responsive coefficient of the system; * denotes complex conjugate; Re() refers to the real part of a complex signal. The third term of the right-hand side of Eq. (2) is the interference term. OCT signal, $I_{\text{OCT}}(z)$, can thus be obtained by performing inverse Fourier transform on $S(k)$:

$$I_{OCT}(z) = \boldsymbol{F}^{-1}\left[S(k) \right] \qquad (3)$$

Denoting the axial point spread function of the OCT system as $h(z)$, which equals $\boldsymbol{F}^{-1}(|E_0(k)|^2)$, we can rewrite Eq. (3) as Eq. (4) with approximation when the bandwidth is relatively small:

$$\begin{aligned} I_{OCT}(z) = \ & \eta h(z) \sum_{i=1}^{3} \left[\left| r a_i \right|^2 + \left| r_{2i} a_i \right|^2 \right] \\ & + \eta \sum_{i=1}^{3} \left[r r_{2i}^* a_i^2 h\left(z - 2L_{i,0} \right) e^{j 2 k_0 \delta l_i} \right] \\ & + \eta \sum_{i=1}^{3} \left[r^* r_{2i} a_i^2 h\left(z + 2L_{i,0} \right) e^{-j 2 k_0 \delta l_i} \right] \end{aligned} \qquad (4)$$

The first term on the right-hand-side (RHS) of Eq. (4) is the auto-correlation term. The second and third terms in the RHS of Eq. (4) represent coherence peaks due to the interference between two end reflectors of each FPI. The second and third term in the RHS of Eq. (4) are symmetry about the zero delay because the Fourier transform is performed on real spectral data.

As indicated by Eq. (4), the change of FPI cavity length δl_i can be extracted from ϕ_i, the phase of OCT signal at delay $L_{i,0}$, which equals $\tan^{-1}\{\textbf{Im}[I_{OCT}(L_{i,0})]/\ \textbf{Re}[I_{OCT}(L_{i,0})]\}$. However, the function $\tan^{-1}$ gives value in the range of $[-\pi/2, \pi/2]$; therefore

$$2 k_0 \delta l_i = \tan^{-1}\left\{ \frac{\text{Im}\left[I_{OCT}\left(L_{i,0} \right) \right]}{\text{Re}\left[I_{OCT}\left(L_{i,0} \right) \right]} \right\} - N_i \pi \qquad (5)$$

$$\delta l_i = \frac{\lambda_0}{4\pi} \tan^{-1}\left\{ \frac{\text{Im}\left[I_{OCT}\left(L_{i,0} \right) \right]}{\text{Re}\left[I_{OCT}\left(L_{i,0} \right) \right]} \right\} - N_i \frac{\lambda_0}{4} \qquad (6)$$

In Eqs. (5) and (6), N_i is the integer that makes $(\delta l_i + N_i \lambda_0/4)$ to fall within the range of $[-\lambda_0/8, \lambda_0/8]$. With small force variation, N_i stays constant. Denoting the first term in the RHS of Eq. (6) as d_i and the second term as $d_{i,0}$ which is assumed to be a constant, we have

$$\delta l_i(F) = d_i - d_{i,0} \qquad (7)$$

When the variation of FP cavity length is large—such that ϕ_i jumps from $-\pi/2$ directly to $\pi/2$ or from $\pi/2$ directly to $-\pi/2$—a phase unwrapping technique can be used to obtain continuous phase or displacement [21].

When a small force is applied to the tool, the change in FP cavity length is extremely small (in the order of a nanometer) compared to the axial resolution of our OCT system—even when the super-elastic material Nitinol is used to fabricate the flexure. Therefore it cannot induce any observable change in the amplitude of OCT signal. Nevertheless, the small displacements can lead to a measurable phase shift of the interference spectrum. In other words, the small deformation can be extracted from the phase of OCT signal at the coherence peaks as shown in Eq. (6), which is demonstrated in the following simulation. In this simulation, we assumed $L_{1,0}$ = 100µm, $L_{2,0}$ = 150µm, and $L_{3,0}$ = 200µm; the light source has central wavelength of 800nm and FWHM bandwidth of 60nm. Superposed spectral interference signals from three FP cavities are simulated and shown in Fig. 2(a) according to Eq. (2). Performing inverse Fourier transform on this interference signal leads to complex-valued spatial domain OCT signal $I_{\mathrm{OCT}}(z)$, which contains three coherence peaks at $z = L_1$, L_2, and L_3 corresponding to the length of the three FP cavities. The amplitude of OCT signal is shown in Fig. 2(b). With force exerted, the
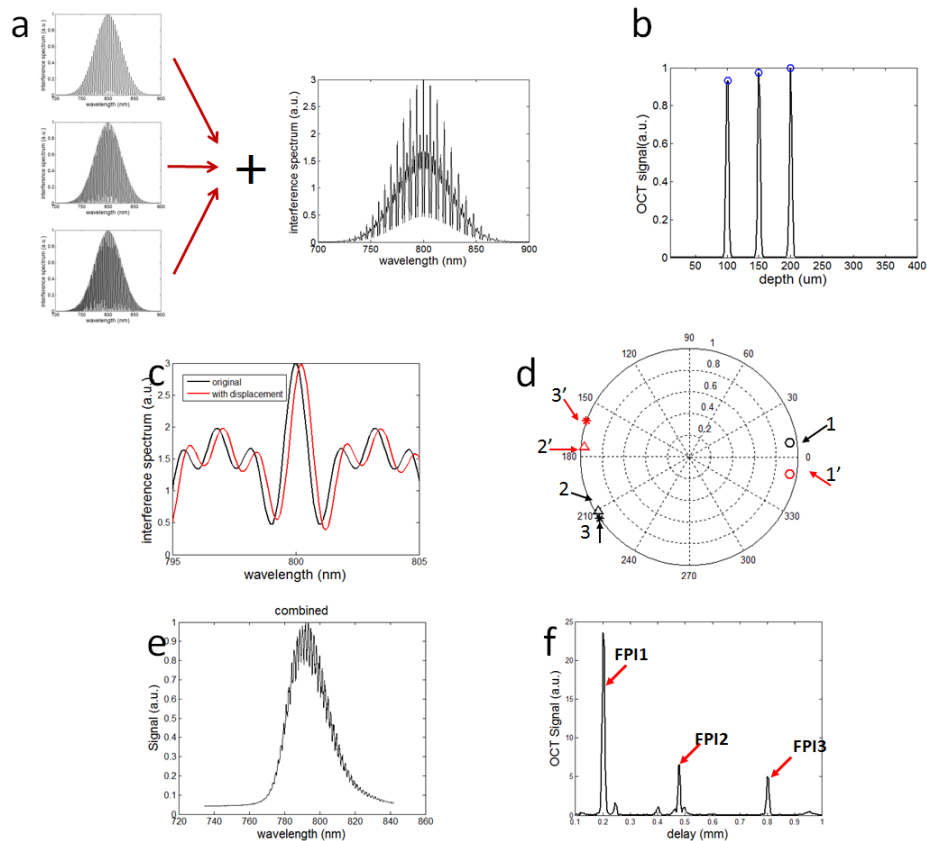

Fig. 2. (a) Superposition of spectral interference signals from three FP cavities; (b) OCT signal with three coherence peaks corresponding to three FP cavities; (c) central part of the interference spectrum: with (red) and without (black) additional displacement δl_i; (d) complex OCT signals at the 1st, 2nd, and 3rd coherence peaks in the complex plane using polar coordinate system. Black symbols and red symbols represent OCT signals with and without additional displacement δl_i; (e) actual interferometric spectrum obtained from the FPI-FS; (f) amplitude of OCT signal obtained by Fourier transforming spectrum shown in Fig. 2(e).

cavity length changed proportionally to the force. In this simulation, we assumed $\delta l_1 = 20$nm, $\delta l_2 = 40$nm and $\delta l_3 = 60$nm. However, such small change in cavity length cannot be seen directly from the amplitude of OCT signal described in Fig. 2(b). On the other hand, as shown in Fig. 2(c) which is the central part of the interference spectrum, change in cavity length in the order of nanometer shifts the original spectrum (black) to the red one. To demonstrate that the small displacement can induce measurable phase change to the complex-valued OCT signal at the coherence peak, we show complex OCT signals at the 1st, 2nd, and 3rd coherence peaks in the complex plane using a polar coordinate system in Fig. 2(d). Black symbols and red symbols represent OCT signals with and without additional displacement δl_i. Clearly, the vector that represents the complex OCT signal rotates due to phase shift induced by δl_i.

In Fig. 2, we also show the actual spectrum obtained from the multiplexed FPIs of our FS as Fig. 2(e). We performed Fourier transform on the interferogram and obtained OCT signal shown in Fig. 2(f). Three peaks in Fig. 2(f) come from interference between end reflectors of the three FP cavities and the locations of these peaks indicate the length of FP cavities.

2.3. 3D force measurement

As demonstrated in the three-dimensional Cartesian coordinate of Fig. 1(b), a force (F) along an arbitrary direction can be decomposed into axial and lateral components. In the force coordinate attached to the tool tip, z axis or axial direction is along the tool shaft. We denote force along the tool shaft direction as axial force F_z. x-y plane is perpendicular to z axis and force in x-y plane is denoted as lateral force F_l. The choice of x and y axes is arbitrary as long as x, y and z axes form a right-hand coordinate system.

As shown in Figs. 3(a) and 3(b), with an axial force applied to the tool, the flexure deforms and the change of FP cavity length is denoted as $\delta l_{i,z}$ which equals $(F_z D)/(A_0 E)$ [25]. Here D is the length of cantilever beam; E is the effective Young's modulus of the cantilever beam; A_0 is the cross-sectional area on which the force is exerted. When lateral force is applied, the beam deflects with an angle α that equals $(F_l D^2)/(2EI)$ where I is the area moment of inertia of the wire cross section [25]. We show the beam deflection with exaggeration in Fig. 3(c). In fact, α is extremely small due to the small force exerted during vitreoretinal microsurgery. Therefore, the slight change in light beam propagation direction does not reduce the coupling efficiency when light gets reflected back to the single-mode fiber and does not reduce the OCT signal amplitude either.

According to Fig. 3(d), the change of FP cavity length $\delta l_{i,l}$ due to lateral force can be expressed as $[-2L_{i,0}\sin^2(\alpha/2)/\cos(\alpha) + b_i\tan(\alpha)]$. As α is extremely small, the following approximation is valid: $\sin(\alpha/2) \approx \alpha/2$; $\tan(\alpha) \approx \alpha$; $\cos(\alpha) \approx 1$. Moreover, $\sin^2(\alpha/2)$ is a higher order term of the already extremely small value α and therefore can be negligible compared to $\tan(\alpha)$. As a result, $\delta l_{i,l} = b_i\alpha$. Here, b_i is the distance between the center of the ith fiber and the neutral surface which is perpendicular to the applied force and passes through the center of the tool shaft cross-section. Denoting the angle between vector F_l and x axis as θ as in Fig. 3(e), we find that b_i equals $(x_i\cos\theta - y_i\sin\theta)$ where (x_i, y_i) is the transversal coordinate of the ith fiber. Therefore b_i can also be expressed as:

$$b_i = \sqrt{x_i^2 + y_i^2} \cos(\theta + \varepsilon_i) \qquad (8)$$

In Eq. (8), $\varepsilon_i = \tan^{-1}(y_i/x_i)$. Assume that the cavity change induced by force F is the linear superposition of the effect of F_z and F_l. In other words, the cavity length change of the ith FP cavity δl_i equals $\delta l_{i,z} + \delta l_{i,l}$ and we can express δl_i as follows:

$$\delta l_i = \frac{F_z D}{A_0 E} + \sqrt{x_i^2 + y_i^2}\, \cos(\theta + \varepsilon) \frac{F_l D^2}{2EI}$$

$$= \frac{D}{A_0 E} F_z + x_i \frac{D^2}{2EI} F_l \cos\theta - y_i \frac{D^2}{2EI} F_l \sin\theta \tag{9}$$

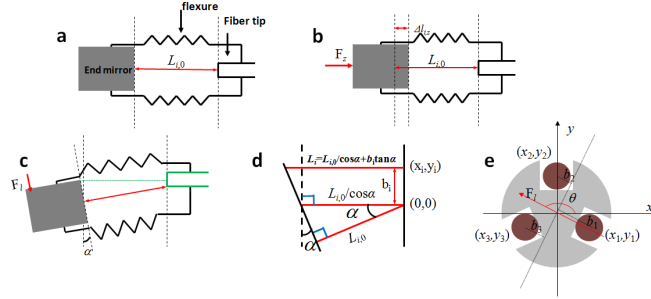It is clear in Eq. (9) that the displacement induced by lateral force has a sinusoidal dependency on θ.

Fig. 3. (a) FS at neutral; (b) axial force changes the length of flexure and changes the FP cavity length; (c) lateral force leads flexure to bend and changes the FP cavity length; (d) diagram shows the calculation of cavity length induced by lateral force; (e) diagram shows the calculation of b_i

Denoting $F_l \sin\theta$ and $F_l \cos\theta$ as F_x and F_y; $D^2 x_i /(2EI)$ and $D^2 y_i /(2EI)$ as A_{ix} and A_{iy}; $D/(A_0 E)$ as A_{iz}, we can re-write Eq. (9) as

$$\delta l_i = A_{ix} F_x + A_{iy} F_y + A_{iz} F_z \tag{10}$$

After introducing F_x and F_y, δl_i is linearly dependent on F_x and F_y with constant coefficients A_{ix} and A_{iy} which are independent of the direction of applied lateral force, as shown in Eq. (9). Therefore, A_{ix}, A_{iy} and A_{iz} can be obtained from a linear regression procedure if we know the force applied to the tool and the corresponding displacements.

Although for a given amplitude of lateral force F_l, F_x and F_y take different values if θ varies, we can always calculate F_l with Eq. (11), which is independent of θ:

$$F_l = \sqrt{F_x^2 + F_y^2} \tag{11}$$

With Eqs. (7) and (10), the relationship between δl_i and F can be shown as follows:

$$\delta \boldsymbol{l} = \boldsymbol{A}\boldsymbol{F} \tag{12}$$

$$\delta \boldsymbol{l} = \begin{bmatrix} d_1 - d_{01} \\ d_2 - d_{02} \\ d_3 - d_{03} \end{bmatrix}; \quad \boldsymbol{A} = \begin{bmatrix} A_{1x} & A_{1y} & A_{1z} \\ A_{2x} & A_{2y} & A_{2z} \\ A_{3x} & A_{3y} & A_{3z} \end{bmatrix}; \quad \boldsymbol{F} = \begin{bmatrix} F_x \\ F_y \\ F_z \end{bmatrix}.$$

Values of elements in matrix $\boldsymbol{A}$ can be obtained from a calibration procedure shown in detail in the following section. Once $\boldsymbol{A}$ is obtained, we are able to calculate the force in three dimension using Eq. (13):

$$\boldsymbol{F} = \boldsymbol{A}^{-1} \delta \boldsymbol{l} \tag{13}$$

As shown in Eq. (12) and Eq. (13), it is critical to subtract d_{0i} from the displacement d_i to obtain correct force measurement. Above d_{0i} is the displacement measured from the phase of OCT signal when no force is applied to the FS. If the subtraction or biasing procedure is taken with a certain force F_0 applied to the FS, the measurement provides force relative to F_0 rather than absolute force.

3. Results

3.1. Axial calibration

In our axial calibration experiment as illustrated in Figs. 4(a) and 4(b), we attached different numbers of testing weights to the FS and maintained the tool shaft in the gravity direction to keep F_x and F_y equal to 0. Therefore, pure axial force along the tool shaft was applied in this setup and coefficients A_{iz} could be obtained. In our calibration experiments, each testing weight was 0.897 ($\pm$ 0.005) mN.

Using the complex-valued OCT signal acquired from our CP-FD-OCT, we calculated the displacements at the three coherence peaks from the phase of OCT signal with Eq. (6) using N_i = 0. The measured displacements are equal to change in the length of FP cavities. With different numbers of testing weights i.e. axial forces, we obtained d_1, d_2, and d_3, displacements corresponding to the three FP cavities, shown as black circles in Figs. 4(c), 4(d) and 4(e), respectively. Afterwards, with the known axial force F_z and the measured displacement $d_i = d_{0i} + A_{iz}F_z$, we were able to perform linear regression to extract A_{1z}, A_{2z}, and A_{3z}. The linear fitting results are shown as red lines in Figs. 4(b), 4(c) and 4(d).
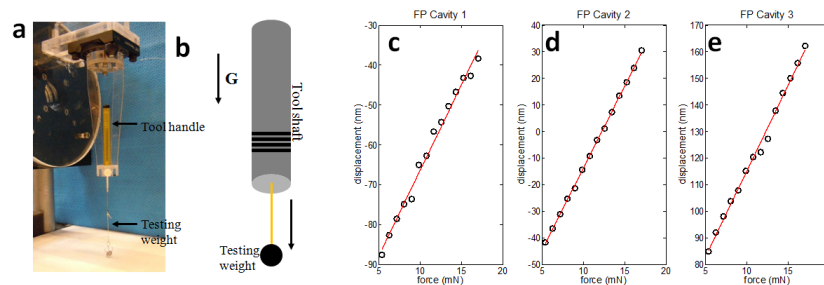

Fig. 4. (a) Photo of axial calibration setup; (b) schematic of axial calibration setup; (c) displacement versus axial force (first FP cavity); (d) displacement versus axial force (second FP cavity); (e) displacement versus axial force (third FP cavity).

3.2. Lateral calibration

In the lateral calibration setup as shown in Figs. 5(a) and 5(b), we maintained the tool shaft (z axis of the force coordinate) perpendicular to the gravity direction so that the force induced by the gravity of the testing weights had only a lateral component in the force coordinate that was attached to the tool tip; in other words, $F_z = 0$. As indicated by Eq. (9), the displacement induced by lateral force not only depends on the magnitude of lateral force exerted to the FS, but also depends on θ, which essentially is the direction of lateral force in x-y plane as shown in Fig. 3 (e). Therefore, to characterize the tool's response to lateral force, we needed to apply force in the lateral plane (x-y plane) with different magnitudes as well as at different azimuth angles θ. In order to do this, we attached the tool to a rotary stage in x-y plane to change the angle between the x axis of our force coordinate and the direction of gravity. Since our force coordinate was attached to the tool tip, θ changes in the same manner as the rotation of the tool.

In our lateral calibration experiments, we attached testing weights to the tool; we rotated the tool circumferentially to obtain different values of θ and took the displacement measurements. We repeated the above procedures with different lateral forces by attaching different numbers of testing weights to the FS. The experimental results of our lateral calibration are shown in Figs. 5(c)–5(e).

Displacements from the 1st, 2nd, and 3rd FP cavities are indicated by circles in Figs. 5(c)–5(e), in which data points with different colors were obtained with different lateral forces (numbers of testing weights are shown as legends in these figures). Figures 5(c)–5(e) clearly indicate that the displacements induced by lateral force vary sinusoidally as the tool orientation θ for a given lateral force, which is consistent with Eq. (9). Sinusoidal fittings of the experimental results are also shown as dashed curves in Figs. 5(c)–5(e) to further verify the functional dependency of displacement on θ. In addition, results in Figs. 5(c)–5(e) also show that the phase of the displacement's sinusoidal dependency on θ varies for different FP cavities. This is because the lead-in fiber for the ith FP cavity takes a different transversal coordinate (x_i, y_i) and therefore the phase $\varepsilon_i = \tan^{-1}(x_i/y_i)$. Moreover, our results also show that the displacements increase proportionally as lateral force increases. To demonstrate this more clearly, in Figs. 5(f)–5(h), we show displacements obtained with different lateral forces when θ was $3\pi/2$. A linear relationship between displacement and lateral force can be observed in Fig. 5(f)–5(h).

To obtain A_{ix} and A_{iy} using data shown in Fig. 5(c)–5(e), we performed a two-dimensional linear regression to solve the linear model $\boldsymbol{d} = \boldsymbol{A}_l\boldsymbol{F}_{xy}$. Here $\boldsymbol{A}_l = [A_{1x}\ A_{1y} ; A_{2x}\ A_{2y} ; A_{3x}\ A_{3y}]$. $\boldsymbol{F}_{xy}$ indicates known vectors with F_x and F_y as elements: $\boldsymbol{F}_{xy} = [F_x ; F_y]; F_x = F_l\cos\theta; F_y = F_l\sin\theta; F_l$
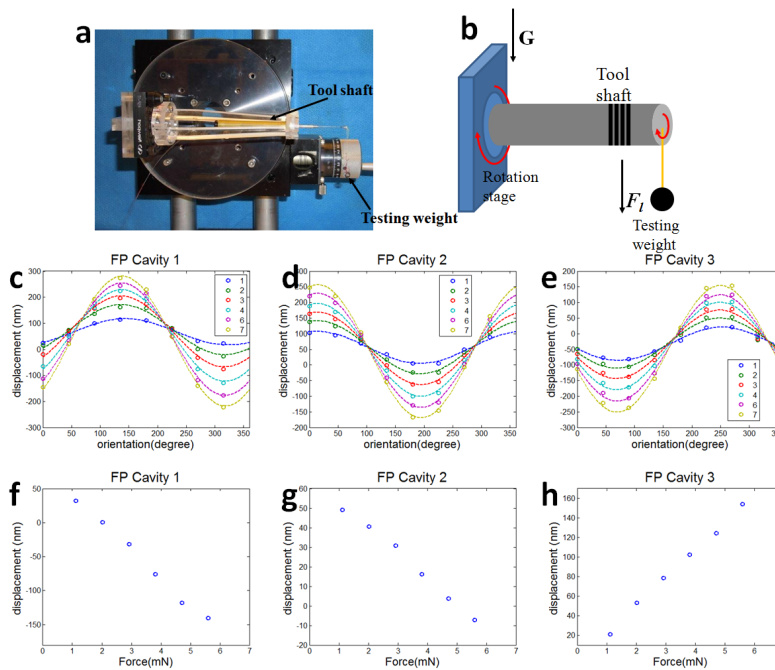

Fig. 5. (a) Photo of lateral calibration setup; (b) schematic of lateral calibration setup; (c)–(h) results from lateral calibration: (c)–(e) show displacements measured from three FP cavities at different θ with different lateral forces. Legends indicate number of testing weights applied to the sensor; (f)–(h) show displacements with different lateral loads when θ was $3\pi/2$.

is the known gravity of testing weights. d indicates the vectors with measured displacements from different FP cavities as elements $d = [d_1; d_2; d_3]$.

With A_l obtained from linear regression of the lateral calibration data, we could calculate F_l inversely. F_x and F_y were obtained by solving the linear equation $d = A_l F_{xy}$ in a least-square manner: $F_{xy} = (A_l^T A_l)^{-1} A_l^T d$. Here $()^{-1}$ indicates to take the inverse of a matrix and $()^T$ indicates to take the transpose of a matrix. F_x, F_y, and F_l extracted are shown in Fig. 6. Only two curves are visible in results with $\theta = 0$ degree, because F_y is almost 0 and therefore F_l is almost overlapped with F_x. Similarly, only two curves are visible in results with $\theta = 90$ degree, because F_x almost is 0. Clearly, although F_x and F_y depend on θ for the same lateral force, F calculated from Eq. (13) is independent of tool orientation, shown as black curves in Fig. 6.
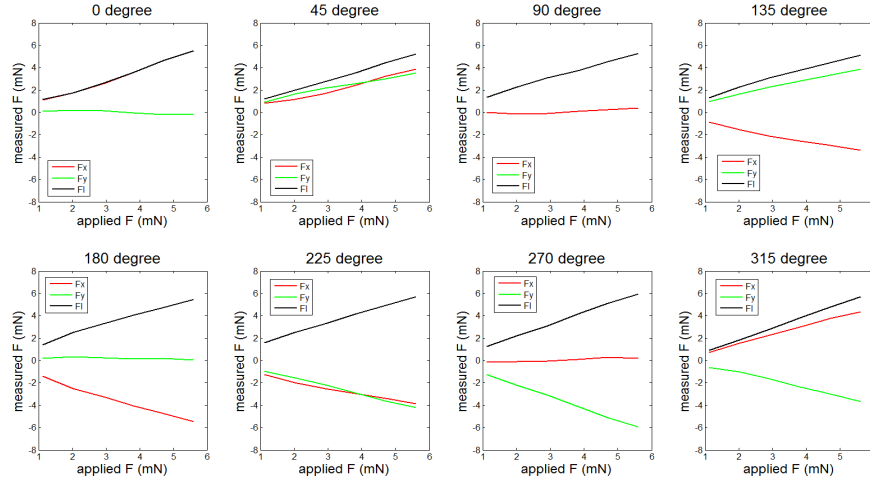

Fig. 6. F_x, F_y and F_l extracted from displacements when θ took different values.

In conclusion, we obtained the following coefficients as elements of our calibration matrix A: $A_{1x} = -30.3\text{nm/mN}$; $A_{1y} = 27.5\text{nm/mN}$; $A_{1z} = 4.3\text{nm/mN}$; $A_{2x} = 33.9\text{nm/mN}$; $A_{2y} = 8.9\text{nm/mN}$; $A_{2z} = 6.2$ nm/mN; $A_{3x} = -11.8\text{nm/mN}$; $A_{3y} = -30.9\text{nm/mN}$; $A_{3z} = 6.5\text{nm/mN}$. $A_{ix} = D^2 x_i /(2EI)$ and $A_{iy} = D^2 y_i /(2EI)$; and x_i and y_i can take different values, positive and negative as shown in Fig. 3(e); therefore, A_{ix} and A_{iy} can take different value and have different signs for the same channel. Force could thus be calculated using Eq. (13) with A and the measured displacements.

3.3. 3D Force measurement

To validate that our FS can measure force with both axial and lateral components, we conducted the following experiment. In addition to the rotary stage in x-y plane, another rotary stage was used to change φ, the intersection angle between the tool shaft and the gravity direction, as shown in Figs. 7(a) and 7(b). With the same load attached to the FS, different values of φ leads to different values of axial and lateral force. Here G is the gravity of the load which equals 8.2mN for this experiment. We used a rotation stage (as indicated by Rotation 1 in Figs. 7(a) and 7(b)) to change φ and therefore change F_x, F_y, F_z correspondingly, because:

$$F_x = G\sin\varphi\cos\theta; F_y = G\sin\varphi\sin\theta; F_z = G\cos\varphi \qquad (14)$$

We repeated the measurements with $\theta = \pi/2$ and $\theta = \pi$. Axial and lateral forces obtained are shown as circles in Figs. 7(c) and 7(d), respectively. Red circles indicate data obtained with $\theta = \pi/2$; blue circles indicate data obtained with $\theta = \pi$.

It is worth mentioning that we biased the displacement reading when $\varphi = \pi/2$ and the FS was exerted with a non-zero force. As shown in Eq. (7) and discussed at the end of Section 2.3, the forces measured were values relative to the force when biasing was taken. As a result, the measured forces are $F_{x,m} = F_x(\varphi)-F_x(\varphi)|_{\varphi = \pi/2}$; $F_{y,m} = F_y(\varphi)-F_y(\varphi)|_{\varphi = \pi/2}$; $F_{z,m} = F_z(\varphi)-F_z(\varphi)|_{\varphi = \pi/2}$. Incorporating Eq. (14), we have $F_{l,m} = G (1-\sin\varphi)$ and $F_{z,m} = G\cos\varphi$, which are also shown in Figs. 7(c) and 7(d) as black curves. The consistency between force measured from our FS and the calculated black curves implies that our FS is able to measure force with both axial and lateral components. With the known load gravity ($G = 8.2$mN), we may bias the data in post processing and obtained the results shown in Figs. 7(e) and 7(f). Results in Figs. 7(e) and 7(f) show maximum axial force and minimum lateral force with $\varphi = 0$; as well as minimum axial force and maximum lateral force with $\varphi = \pi/2$.
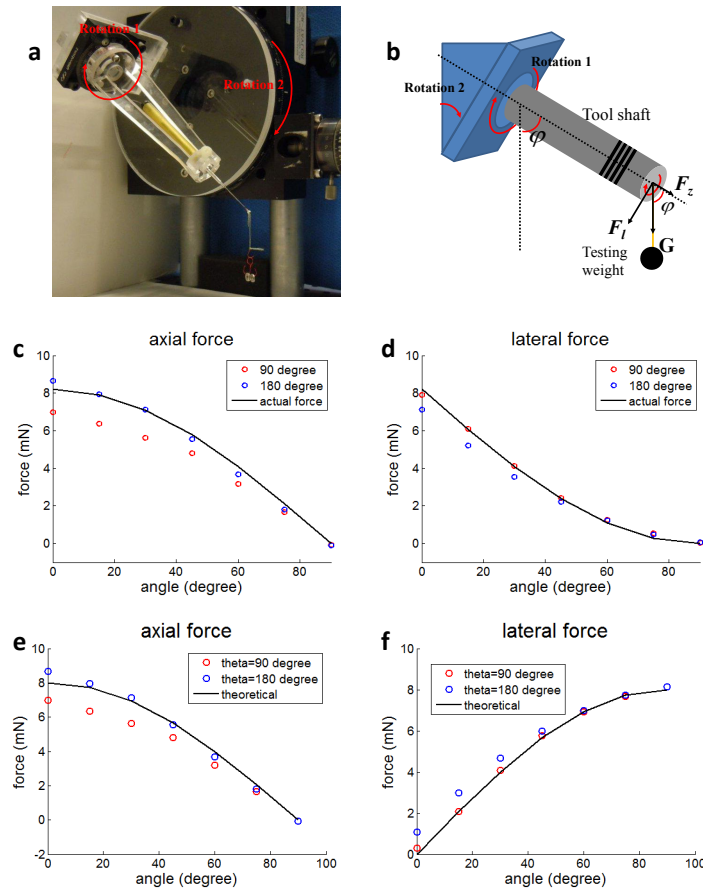

Fig. 7. (a) Photo of 3D force measurement setup; (b) Schematic of 3D force measurement setup; (c) Measured and actual axial force; (d) Measured and actual lateral force; (e) Measured and actual axial force obtained by using the known load gravity as bias; (f) Measured and actual lateral force obtained by using the known load gravity as bias.

4. Discussion

Measuring a force in an arbitrary direction with respect to the tool shaft of the FS requires at least three FP cavities to provide independent displacement readings. First, the change of FPI cavity length is a linear superposition effect of axial and lateral forces. As indicated by our calibration experiments, the same magnitude of lateral force can induce much larger change in

cavity length compared to axial force. In other words, our FS's response to axial and lateral forces are very different. Therefore, it is necessary to differentiate F_z and F_l. Second, the displacement introduced by lateral force F_l is angle (θ) dependent, as shown in Eq. (9). As a result, it is more convenient to decomposition F_l in x-y plane as F_x, F_y and afterwards use Eq. (11) to calculate F_l, which would be independent of the choice of x or y axis of our force coordinate. As we need to determine three unknowns—F_x, F_y, and F_z—it requires at least three independent linear equations based on measurements from three different FP cavities.

As discussed in Section 2.3, we can directly calculate our FS's response to axial and lateral forces using the mechanical and geometric properties of our tool. However, the mechanical property of flexure might change significantly because Nitinol changes its mechanical property during laser cutting procedures. Moreover, we applied medical adhesive to glue different components together, which would also change the overall mechanical properties of the tool. Besides, due to the extremely small dimension of the tool, the geometry of the fabricated tool might be different from the initial design. As a result, experimental calibration can characterize the performance of our FS much better than a theoretical model or even finite element analysis.

Our calibration results show that different FP cavities have different responses to axial force (A_{1z} = 4.3nm/mN; A_{2z} = 6.2nm/mN; A_{3z} = 6.5nm/mN). However, as indicated by Eq. (9), the sensitivity of our FS to axial force should be identical for different FP cavities because $A_{iz} = D/(A_0 E)$. The difference in axial sensitivity might be due to the asymmetry in mechanical property of our FS. Similarly, lateral sensitivity $(A_{ix}^2 + A_{iy}^2)^{1/2} = D^2 r/(2EI)$ should be the same for different cavities as in Eq. (9); however, our experimental values are 43.2nm/mN, 35.0nm/mN, and 33.1nm/mN for the first, second, and third FP cavities, respectively. The difference in the lateral force sensitivities might be the result of the asymmetry in mechanical property of our FS, as well as the misalignment of the fibers. Due to the extremely small scale of our tool, it is almost impossible to make sure that the fibers have the same distance to the center of the tool shaft to make $(A_{ix}^2 + A_{iy}^2)^{1/2}$ identical for the three FPIs.

The force measurement sensitivity depends on the sensitivity of phase-resolved displacement measurement as well as A, coefficients relating cavity length change, and force. According to Eq. (13), the variance of force $\sigma_F^2 = \text{Var}(F)$ can be calculated from the covariance matrix of Gaussian random vector δl, $\text{cov}(\delta l)$: $\text{cov}(F) = A^{-1}\text{cov}(\delta l)[(A^{-1})^{\text{T}}]$, and σ_F^2 is the diagonal elements of the matrix $\text{cov}(F)$ [26]. To estimate the magnitude of σ_F^2, we further assume δl_1, δl_2, δl_3 are independent random Gaussian variables with the same variance σ_l^2. This simplifies the expression of σ_F^2, which becomes $\sigma_F^2 = \sigma_l^2 A^{-1}[(A^{-1})^{\text{T}}]$. Although the fundamental lower limit of σ_l is determined by the signal-to-noise ratio (SNR) of the OCT system [17], phase or displacement fluctuation due to environmental disturbances such as temperature variation and air flow is slower but larger in magnitude, and therefore determines the sensitivity of force measurement. In our experiment, σ_l was 0.5nm from a long-term (10s) measurement while σ_l was 0.1nm from a short-term (0.5s) measurement. Using σ_l = 0.5nm and the obtained calibrating matrix A, we were able to calculate $\text{cov}(F)$ and further extract σ_F: $\sigma_{Fx}\approx$0.01mN; $\sigma_{Fy}\approx$0.01mN; $\sigma_{Fz}\approx$0.05mN. There results indicate that our FS can achieve sub-millinewton sensitivity in force measurement.

As shown in Eq. (5) and Eq. (6), we extract displacement from the phase of a complex number that is defined in the domain [$-\pi/2$ $\pi/2$]. When a time-varying phase reaches and crosses the boundary of this range, the phase calculated from Eqs. (5) and (6) will show an abrupt change of $\pm\pi$, depending on whether the phase decreases or increases. According to Eq. (7), the value of d_i is from -100nm to $+100$nm and therefore we can obtain displacement without ambiguity only in a range of 200nm. Since our FS has 30 ~40 nm/mN sensitivity to lateral force, a 200nm displacement range allows us to measure 5mN ~6mN lateral force at most. Therefore, a severe restriction in the dynamic range of our force measurement is placed by the limited range of displacement measurement. However, we implemented a well-established method

called *phase unwrapping* in this work to increase the dynamic range of our force measurement [16]. In our C++ software, we continuously calculate the phases corresponding to each coherence peak and check whether there is an abrupt change of $\pm\pi$ between two consecutive phases: ϕ_n, ϕ_{n+1}. If such phase discontinuity occurs, we modify the phases obtained after ϕ_n by subtracting or adding π. This method can increase the dynamic range in the measurement of displacement and thus force, because the force is assumed to be continuous and usually cannot lead to such a big change in ϕ due to the short time between two sampling points (1ms). However, if the force varies quickly (dF/dt>5mN/ms), the unwrapping technique cannot provide correct force measurement.

5. Conclusion

In this study, we proposed and studied a miniature fiber-optic force sensor based on low coherence Fabry-Pérot interferometry for vitreoretinal surgery. We used a common-path Fourier domain optical coherence tomography to interrogate the change of FP cavity length through phase-sensitive detection. We fabricated a force sensing tool with an outer diameter less than 1 mm. Calibration was performed to characterize the tool. We also conducted experiments to verify that our FS can measure force with both axial and lateral components.

Acknowledgments